# The Vertical Structure of TOGA COARE Convection. Part II: Modulating Influences and Implications for Diabatic Heating

CHARLOTTE A. DEMOTT AND STEVEN A. RUTLEDGE

*Department of Atmospheric Science, Colorado State University, Fort Collins, Colorado*

(Manuscript received 10 September 1996, in final form 15 December 1997)

ABSTRACT

The temporal variability of western Pacific warm pool convection, especially its vertical structure, is examined in this study. Distributions of convective echo top heights and 30-dB*Z* contour heights have been produced from shipboard radar data collected during Tropical Ocean Global Atmosphere Coupled Ocean–Atmosphere Response Experiment (TOGA COARE). Elevation and suppression of convective heights was primarily influenced by the phase of the intraseasonal oscillation (ISO), with heights being suppressed during convectively inactive and westerly wind burst (WWB) phases of the ISO. Echo top heights were greatest during the convective phases and post-WWB phases of the ISO. However, at least some very deep convection was always present within the area observed by radar, indicating that local conditions were favorable for deep convection, even when the large-scale environment was not capable of supporting widespread deep convection. In addition to the ISO, echo top and 30-dB*Z* contour heights were also influenced over shorter timescales by intrusions of dry subtropical air into the COARE Intensive Flux Array (IFA). Periods of convective suppression were also accompanied by upper-tropospheric drying.

Convective diabatic heating profiles, computed from a combination of surface radar and sounding data, reveal that the shape of the monthly mean heating profiles varied over the four-month intensive observing period. Maximum heating occurred at the highest elevations during the convectively inactive phases of the ISO, and at the lowest elevations during the convectively active phases of the ISO. These variations are qualitatively consistent with higher (lower) convective available potential energy values and higher (lower) 30-dB*Z* contour heights above the freezing level during the strong surface easterly (westerly) phase of the ISO. Factors leading to widespread convective suppression despite the presence of a high environmental CAPE are also discussed.

## 1. Introduction

The vertical distribution of hydrometeors in tropical precipitating systems impacts longwave and shortwave radiation budgets (Wong et al. 1993), diabatic heating profiles (Lau et al. 1989), and lightning production (Lhermitte and Williams 1985; Petersen et al. 1996). Over the past decade or so, observations have yielded insights into how convective-scale hydrometeor distributions, vertical motion, heating profiles, and lightning production in the Tropics are all interrelated, as well as how various large-scale factors influence their behavior. Knowledge of these interactions in tropical regions is of particular interest owing to the disproportionately large amount of diabatic heating that takes place in tropical latitudes.

Vertical motions initiate phase changes of water that result in microphysical processes, which, to a first approximation, determine diabatic heating profiles. Convective diabatic heating is usually positive over the depth of the atmospheric column, although it is sometimes negative near the surface owing to effects of evaporative cooling. In contrast, in stratiform precipitation, vertical motions are typically small compared to hydrometeor fall speeds, so hydrometeors fall, relative the broad and quasi-horizontally uniform updraft. In this situation, hydrometeor growth takes place in the upper levels of the cloud through deposition and aggregation. As the ice crystals fall through the freezing level, they melt and usually begin to evaporate, resulting in a heating profile that is positive in the upper levels and negative at lower levels. These concepts have been developed by many authors and recently reviewed by Houze (1989).

Fundamental differences between continental versus tropical oceanic vertical motion profiles (that lead to fundamentally different heating profiles; Johnson and Young 1983) were presented by Zipser and LeMone (1980) in a comparison of aircraft-sampled vertical velocity data from the continental Thunderstorm Project (Byers and Braham 1949) and tropical GARP (Global Atmospheric Research Program) Atlantic Tropical Experiment (GATE). Their analyses revealed that oceanic convective updraft velocities were uniformly weaker

*Corresponding author address:* Dr. Steven A. Rutledge, Department of Atmospheric Science, Colorado State University, Fort Collins, CO 80523.
E-mail: rutledge@olympic.atmos.colostate.edu

© 1998 American Meteorological Society

than their continental counterparts at all levels, as fewer than 10% of all tropical updrafts reached velocities comparable to the median continental updraft velocity. Subsequent analyses of tropical updraft velocities from other locations revealed similar results (e.g., Jorgensen and LeMone 1989; Lucas et al. 1994). Zipser and LeMone (1980) discussed the implications of this updraft structure on microphysical processes. For even the strongest tropical updrafts, the time required for a parcel to travel from cloud base to the freezing level is about 20 min; median updraft speeds extend this to approximately 1 h. Assuming a maritime droplet spectrum, this is sufficient time for rain to be generated by collision-coalescence processes, acquire fall speeds greater than the updraft velocity, and fall back to the surface. Similarly, the weak updrafts above the freezing level allow conversion from liquid water to ice particles over a relatively short distance. The large amount of water mass below the freezing level and the relative scarcity of supercooled liquid water aloft are consistent with the rapid decrease in radar reflectivity with height above the freezing level in the Tropics.

Szoke et al. (1986) investigated the arguments of Zipser and LeMone (1980) by comparing convective core reflectivity profiles of continental and oceanic systems. For oceanic systems, the reflectivity profiles were nearly constant from the surface up to the freezing level, at which point they decreased rapidly with height. In contrast, continental profiles often increased with height and reached their maximum values well above the freezing level. This difference in reflectivity profile shape between the two regions was attributed to differences in the buoyancy profile. In the Tropics, buoyancy is often distributed quasi-uniformly with height, so that acceleration is weak but constant throughout the parcel's ascent, thus allowing the microphysical processes discussed above to take place. In contrast, buoyancy in the midlatitudes is often concentrated at low levels, resulting in large accelerations of lifted parcels, strong vertical velocities, and thus short ''travel times'' from below to above the freezing level. This sequence leads to higher concentrations of supercooled liquid water aloft, promoting larger ice water contents and radar reflectivities above the freezing level.

Differences in internal storm structure may be linked to a system's electrical activity. Lightning observations are often a good indicator of updraft strength and microphysical makeup since its production is thought to be most efficient in a cloud environment between 0°C and −20°C that is characterized by both ice particles and water droplets (i.e., Takahashi 1978). Several recent multiparameter radar and in situ studies lend further evidence supporting the relationship between updraft strength, microphysical composition, and electrical behavior (i.e., French et al. 1996; Jameson et al. 1996; Ramachandran et al. 1996; Carey and Rutledge 1996).

Rutledge et al. (1992) analyzed lightning flash rates during the 1988–89 wet season near Darwin, Australia, as part of the Down Under Doppler and Electricity Experiment (DUNDEE). Flash rates increased during periods of high environmental convective available potential energy (CAPE) associated with southeasterly flow when the monsoon trough was north of Darwin (the continental or monsoon ''break'' regime), and decreased during the periods when the trough was south of Darwin and flow was from the northwest (the monsoon regime). Zipser and Lutz (1994) analyzed radar reflectivity ''lapse rates'' (the rate of reflectivity decrease with height) above the freezing level of convective cores from break and monsoonal convection observed during DUNDEE and found that monsoonal cores had much larger lapse rates above the freezing level compared to those of the monsoon break (i.e., continental) regime.

Taken together, the above-described findings circumstantially confirm the link between microphysical processes, radar reflectivity, vertical motion profiles, and lightning production. Furthermore, because diabatic heating profiles are to a first approximation proportional to vertical motion profiles (Johnson and Young 1983), the microphysical structure and electrical characteristics of convection may also be indicative of convective heating profile shape, which is thought to play an important role in determining the overall heating profile shape of precipitating systems (Houze 1989).

Because the vertical structure of convective echo and resulting convective heating profiles in the Tropics are more variable than those of stratiform echo (Houze 1989), it is important to continue to examine the variability in vertical structure of tropical convection. To this end, monthly distributions of convective echo and its contribution to the total convective rainfall observed during Tropical Ocean Global Atmosphere Coupled Ocean–Atmosphere Response Experiment (TOGA COARE) were presented in Part I of this study. Part II focuses on the higher-frequency variability of convection, the environmental factors that appear to regulate the variability, and explores its relation to convective diabatic heating profiles.

## 2. Data processing and experiment review

The Massachusetts Institute of Technology (MIT) radar was deployed aboard the R/V *Vickers* for three 30-day cruises during COARE to the nominal position 2.08°S, 156.25°E within the intensive flux array (IFA). Full-volume radar data (at 20-min resolution) were interpolated to a 240 km × 240 km × 18.5 km Cartesian grid with 2 km × 2 km × 0.5 km grid boxes centered on the radar. The data were partitioned into convective and stratiform echo populations; rainfall rates were then computed by applying two separate $Z$–$R$ relations to each echo type at a height of 2 km. Daily rainfall rates were computed by summing the 20-min resolution rain amounts.

A time series of radar-derived daily rainfall rates as

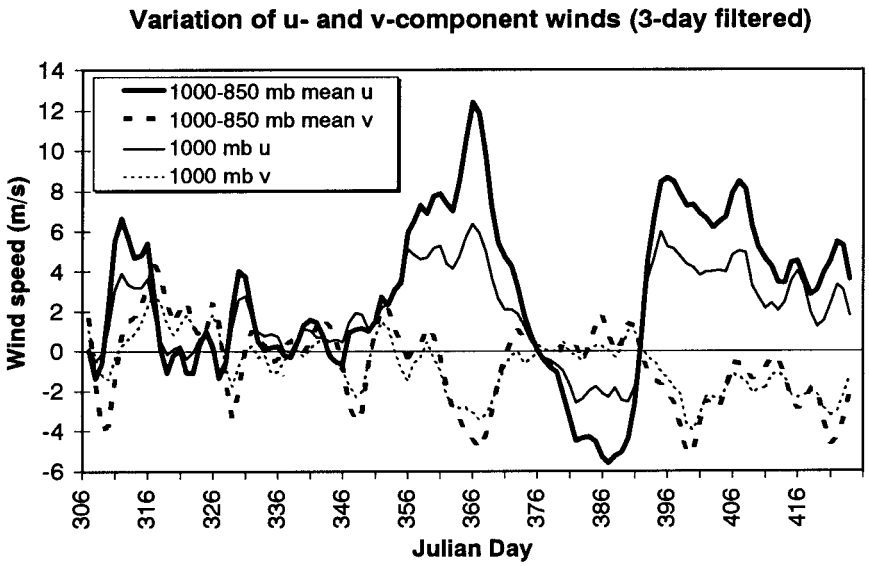


FIG. 1. Time series of IFA mean zonal $u$- (solid) and $v$- (dashed) component winds at 1000 mb (light lines) and averaged over 1000 to 850 mb (heavy lines). A three-day running mean has been applied to the data.

well as several variables diagnosed from the COARE sounding network (Lin and Johnson 1996a) were presented in Fig. 2 of Part I of this study. This time series illustrates the passage of three cycles of the 30–60-day intraseasonal oscillation (ISO). The convective phase of the first ISO made its way through the IFA on 10–11 November 1992 (Julian days 315–316). After a few days of moderate westerly winds, the remainder of cruise 1 was dominated by the convectively inactive portion of the ISO and experienced the calmest seas and most ''suppressed'' conditions of any of the three cruises. The second cruise, which began on 21 December 1992 (Julian day 356) coincided with the second and most well-defined passage of the ISO on 24–25 December 1992, followed by several days of strong surface winds and unorganized convection. As the strong surface westerly phase (frequently referred to as a westerly wind burst, or WWB) of this passage subsided, convective activity increased, then once again decreased as another inactive phase of the ISO settled into the IFA. The third cruise, which began on 29 January 1993 (Julian day 395[1]), initially sampled the WWB following the convective phase of the ISO, and then remained in somewhat weaker westerly flow characterized by a steady succession of convective events.

## 3. Temporal variability of convective vertical structure

Part I of this study presented monthly distributions of convective grid column heights and 30-dB$Z$ contour heights and the rainfall associated with these grid columns.[2] Such distributions provide insight to the magnitude of variations that can be expected over monthly timescales. However, atmospheric disturbances with shorter timescales are frequently observed in the western Pacific warm pool region. It is of interest then, to examine how distributions of convective properties vary from day to day and to relate the observed variations to large-scale conditions.

### *a. Daily variations of convective distributions*

Reasons for observed variations in convective distributions may be more easily understood when placed in the context of previously identified atmospheric phenomena. In this subsection, convective variability is discussed primarily in terms of the ISO, whose progression is particularly well identified by the time series of near-surface zonal wind speeds, presented in Fig. 1. As Lin and Johnson (1996a) illustrated, westerly surface winds intensify as the main convective phase of the ISO approaches from the west, and can increase dramatically west of the main convective phase. Surface westerlies steadily decrease in the days following a WWB, and often reverse to weak to moderate easterlies for a brief period before returning to westerlies in advance of the next passage of ISO convection. The time series of Fig. 1 reveals that westerly surface winds are about twice as common as easterlies, so they represent more than half

[1] 366 has been added to 1993 Julian days for continuity purposes.

[2] Recall that all analysis of ''convective echo'' is based on partitioned echo. In other words, stratiform echo is not included in the analysis.

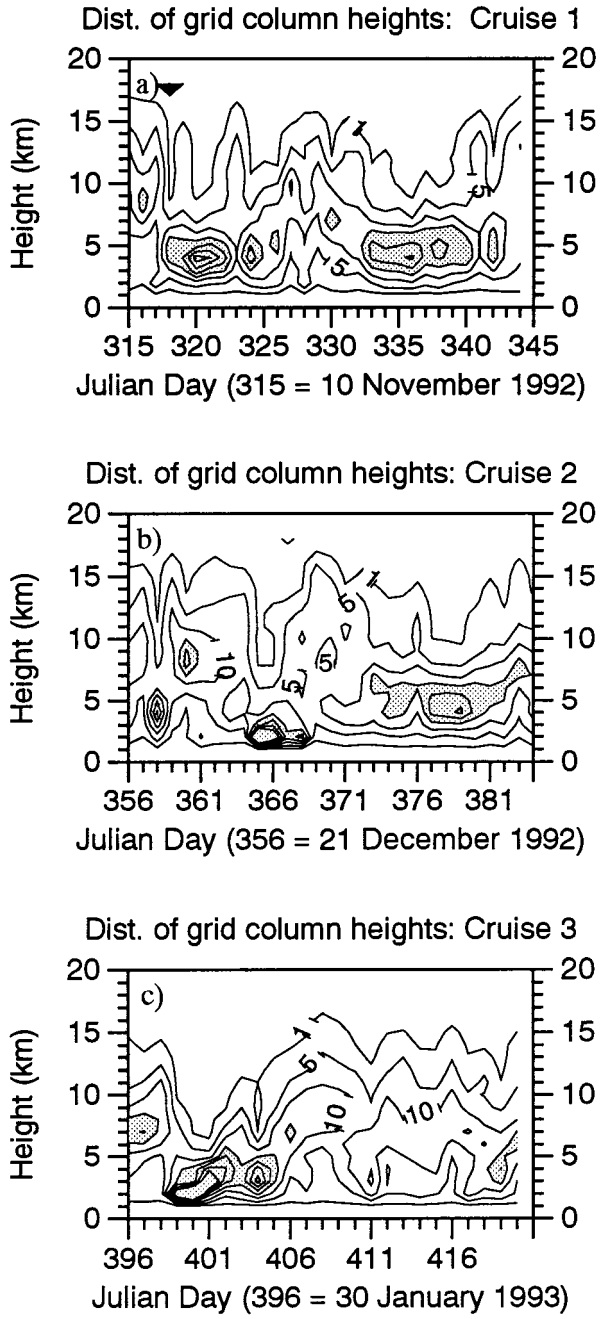


FIG. 2. Relative frequency distribution of convective grid column heights for cruises 1, 2, and 3. Relative frequencies are contoured at 1%, 5%, 10%, 20%, 30%, and 40%. Frequencies greater than 20% are shaded.

of a single ISO wavelength. However, by considering the time series of radar-identified convective echo, and wind speed, as well as direction, it is possible to identify the preconvective, convective, and WWB periods contained in westerly flow.

Time–height relative frequency distributions of convective grid column heights for each cruise are presented in Fig. 2. Relative frequencies greater than 20% are shaded. For example, on Julian day 335, the 4–5- and 5–6-km feature height bins (Fig. 2a) each contain more than 20% of all observed features. A cross section along any Julian day in Fig. 2 when viewed along the Julian day axis would resemble a frequency distribution bar chart, such as those shown in Part I of this paper, with feature height on the ordinate and relative frequency on the abscissa. Shaded areas would correspond to the taller bars (higher frequencies). The distributions of grid column height can vary substantially over periods shorter than one week. Note that, although the modal height varies with time, at least some very deep convective features were always present.

The first few days of cruise 1 (Julian days 315–317) sampled convection associated with a weak convective phase and WWB. Convective grid column heights are grouped between 5 and 15 km, with very few column heights found below 5 km. On Julian day 318, the convective phase of the ISO moved east of the MIT radar and surface winds decreased. This transition was accompanied by a sudden shift in the distributions to lower heights. The grid column distribution shows a modal height during this period of about 4 km. The extended period of shallow convection that was present during most of cruise 1 was interrupted around Julian days 326 through 332, during which time daily rainfall rates (see Fig. 2, Part I) and convective heights increased dramatically. This brief active period was accompanied by an increase in surface westerlies. The second period of suppressed convection during cruise 1 (Julian days 333–342) was accompanied by weak easterly surface flow. As the surface winds began to shift from easterly to westerly with the approaching ISO, convection again became more intense.

Cruise 2 captured both the convective and strong surface westerly phases of the ISO, as well as several days of the inactive phase. The most intense convective activity and highest daily rain rates of the entire intensive observing period (IOP) occurred on Julian day 360. Convective column modal heights were about 8 km. A particularly strong WWB followed the passage of the convective phase, which coincided with shallow convection with echo top heights confined well below the freezing level.[3] The lower sea surface temperatures that resulted from the strong mixing associated with the WWB may have also acted to suppress convective development. As the surface westerlies and tropospheric shear decreased, and sea surface temperatures began to recover, conditions once again became favorable for deeper convection up until approximately Julian day

[3] Some of the features and grid columns identified during this period (Julian days 365–368) are actually sea clutter, which could be observed up to heights of 2 km in the gridded data. The partitioning algorithm generally eliminated most of the sea clutter from the convective partition, the exception being the small ring of high reflectivities within a few kilometers from the radar.

372. By this time, the inactive phase of the ISO had entered the IFA and convective heights decreased.

The first several days of cruise 3 were convectively active with the approach of the convective phase of another ISO. However, the bulk of the convective activity leapfrogged the IFA (Chen et al. 1996), resulting in a quick transition from convective phase to WWB on Julian day 400. As with the WWB in cruise 2, convective heights were drastically suppressed compared to their distribution during the remainder of the cruise. Once again, however, as the tropospheric shear associated with strong low-level winds decreased during early February (around Julian day 406), conditions became more favorable for convective activity. The remainder of cruise 3 was characterized by relatively strong westerly winds, suggesting a prolonged WWB phase with this ISO passage. An inactive phase such as those observed during cruises 1 and 2 was never observed and, consequently, convective echo tops remained high.

How did the internal structure of convection vary during each cruise? Time-height relative frequency distributions of convective grid column 30-dBZ contour heights are presented in Fig. 3. In general, the temporal trends of 30-dBZ contour height distribution are similar to those for echo top height in Fig. 2, with more grid columns being vertically intense (as indicated by their 30-dBZ contour height) during periods of enhanced rainfall, and less intense during WWBs and inactive phases of the ISO. The tendency for the majority of convective grid columns having 30-dBZ contour heights below the freezing level (situated at approximately $z = 4.5$ km), even during relatively active periods, is apparent. The modal 30-dBZ column height of convective grid columns rarely exceeds 4 km during cruise 2, whereas the modal 30-dBZ contour height during cruises 1 and 3 surpasses the 4-km mark on several days. This behavior is consistent with the monthly mean characteristics of convection presented in Part I.

The temporal evolution of the distribution of rainfall as a function of echo top height for each cruise is presented in Fig. 4 and reveals some interesting insights into the cruise-mean distributions presented in Part I. For example, it is now seen that the bimodal distribution of convective rainfall production seen during cruise 1 was indeed accomplished by two populations of convective echo, but these populations did not exist simultaneously. Instead, convective rainfall fell primarily from grid columns with tops between about 8 and 15 km for most of cruise 1, but rainfall production shifted to more shallow convection on Julian days 318 and 333 through 339. Convective rainfall during the strong ISO passage of cruise 2 was broadly distributed over the height bins above the freezing level. Interestingly, the grid column distribution reveals that rainfall production by the very tallest grid columns peaked after the ensuing surface westerlies had subsided, and not during the main convective burst of the ISO. The presence of the more shallow cloud population seen in cruise 1 is suggested

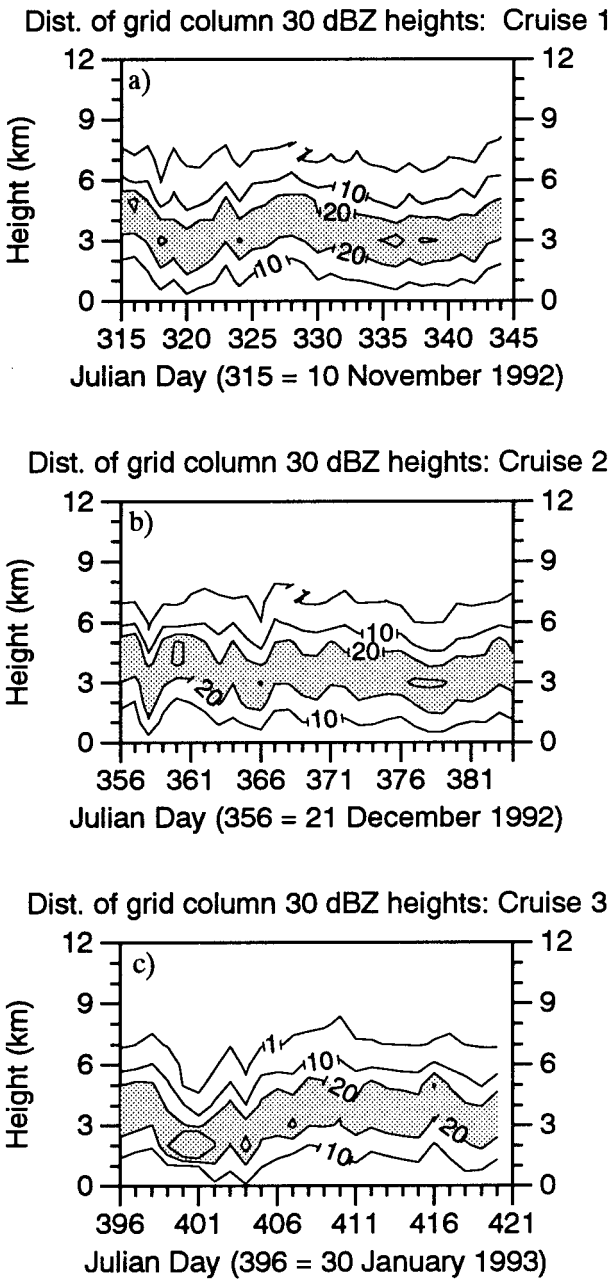


FIG. 3. As in Fig. 2 but for 30-dBZ contour heights. Relative frequencies are contoured at 1%, 10%, 20%, and 30%.

during the inactive period of cruise 2 (Julian days 374–380), but is masked in the cruise mean distributions by the enormous amounts of rain that fell in the first 10 days of the cruise. Rainfall production as a function of echo top height varied little during cruise 3, except on Julian day 400 when almost no rain fell.

Finally, rainfall production as a function of 30-dBZ contour height is presented in Fig. 5. The reduced variability of 30-dBZ contour height distributions seen in Fig. 3 is reflected in the rainfall distributions. Even dur-

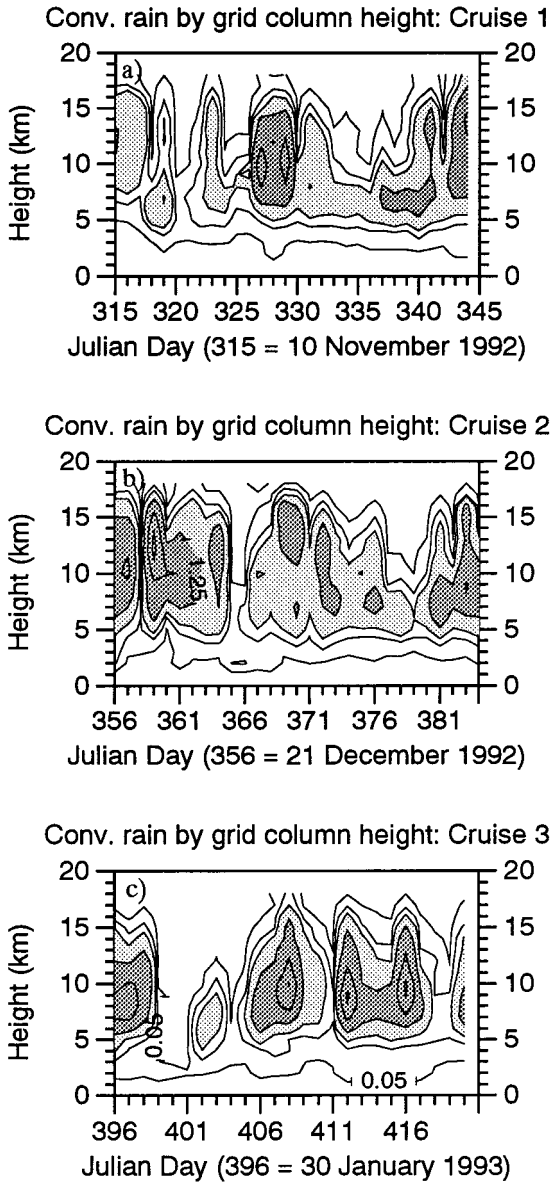


FIG. 4. Distribution of rainfall contribution as a function of convective grid column height for each cruise of the R/V *Vickers*. Rainfall units are mm $h^{-1}$ and are contoured at intervals of .05, 0.25, 0.5, 1.25, 3.0, and 5.0. Fluxes greater than 0.5 mm $h^{-1}$ are lightly shaded, while those greater than 1.25 mm $h^{-1}$ are dark shaded.

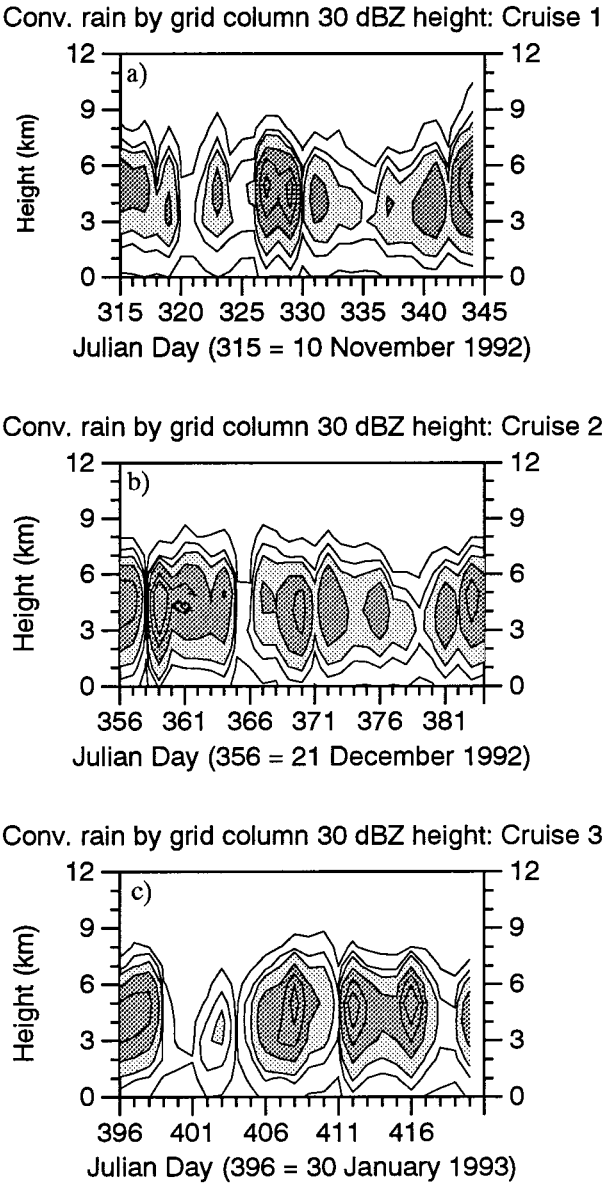


FIG. 5. As in Fig. 4 but for 30-dBZ contour heights.

ing the extremely suppressed conditions of cruise 1 (Julian days 333–339), the modal rainfall height decreased only to about 4 km compared to about 5 km for the rest of the cruise. The rainfall by height distributions were broadest toward the end of cruise 1, and following the surface westerly wind periods of cruises 2 and 3 (Julian days 367–369 and 407–410), indicating the presence of more vertically intense features at these times. Interestingly, the distributions of rainfall as a function of 30-dBZ contour height during the main convective phase of each ISO (Julian days 315–317, 359–361, and 396–397) are narrower and more peaked than the postsurface westerly distributions (date ranges given above), suggesting that the most vertically intense convection during COARE occurred 2–3 days following strong surface westerlies, rather than the few days preceding them.

### *b. Convective vertical structure and tropospheric moistening*

This section focuses on the modulation of convective activity by intrusions of dry subtropical air advected into the IFA at low levels by rotating disturbances and how this behavior interacts with modulation by the ISO disturbance scale. While convection is clearly modulated by the ISO, several authors (Reed and Recker

1971; Numaguti et al. 1995; Takayabu et al. 1998; Haertel and Johnson 1998) have demonstrated that convection is also modulated on shorter timescales by rotational disturbances such as 2-day and 4–5-day waves. The 4–5-day waves have been observed to occasionally advect ''tongues'' of dry subtropical air into the Tropics by ''entraining'' filaments of this air into their circulation patterns and then advecting this air equatorward. These dry tongues typically have bases 1.5–2.0 km above the surface and may suppress convection by both stabilizing the atmosphere aloft and by rapidly evaporating any moist convection that penetrates the base of the dry layer. The behavior of these dry tongues has been discussed more extensively by Numaguti et al. (1995), Yoneyama and Fujitani (1995), and Mapes and Zuidema (1996). The time series plots of meridional wind (Fig. 1) illustrate the presence of rotational disturbances with timescales shorter than those associated with the 30–60-day ISO cycle (e.g., as seen in the 1000–850-mb mean $v$-component wind during Julian days 330–350). Figure 6b shows the variation of low-level wind speed and rainflux-weighted echo top heights. Rainflux (the volume of rain falling from echo over a fixed period of time) was computed by assuming that the instantaneous rainfall rates computed from the *Z-R* relation were constant over the 20-min sampling period. Daily mean flux-weighted heights were computed as follows:

$$\text{Flux-weighted height} = \overline{\left( \frac{\sum_{\text{columns}} \text{flux} \times \text{height}}{\sum_{\text{columns}} \text{flux}} \right)}, \quad (1)$$

where the overbar represents averaging over all radar volumes analyzed in a given day.[4]

Analysis of convective vertical structure modulation by rotational disturbances and their associated dry ''tongues'' is somewhat more complicated than that for the ISO for several reasons. First, not all rotating disturbances advect dry air into the IFA. Second, widths of the dry air filaments can be quite narrow (i.e., a few hundred kilometers), and therefore not well-resolved by the sounding network (Mapes and Zuidema 1996). Furthermore, because these dry air filaments are ''entrained'' into the rotating disturbances, they are not preferentially associated with any particular low-level wind direction [see the time series of two such dry air intrusions in Numaguti et al. (1995)], so an analysis of convective vertical structure as a function of meridional wind speed or direction produces ambiguous results. Therefore, modulation of convective vertical structure by dry air intrusions is described for those cases presented in the literature.

The first dry air intrusion to the IFA while the R/V *Vickers* was on station occurred on 13 November 1992 (Julian day 319). Mean relative humidities with (computed with respect to water) in the 1000–500-mb layer (hereafter referred to as low-level relative humidity) dropped from over 70% on 12 November to less than 55% on 13 November (Fig. 6a), whereas 500–350-mb mean relative humidity (hereafter referred to as upper-level relative humidity) also dropped nearly simultaneously (note that two separate vertical axes are used in Fig. 6). Rainflux-weighted grid column heights decreased from a maximum of 13 km just a few days prior, to just over 8 km upon arrival of the dry air. By 15 November 1992 (Julian day 321), low-level relative humidity had recovered to about 65%, whereas upper-level humidity recovered at a somewhat slower rate. The time height cross section of tropospheric relative humidity (Fig. 7) reveals that the low-level relative humidity increase was primarily driven by a gradual erosion (moistening) of the moisture inversion base with time. At the same time, the flux-weighted height of convective grid columns was increasing.

The scenario of tropospheric drying at lower and upper levels, convective suppression, and then gradual tropospheric moistening associated with the increase in convective intensity raises questions as to how each of these processes is regulated. Since dry tongues have been tracked backward in time to subtropical origins (i.e., Numaguti et al. 1995; Ushiyama et al. 1995), it is clear that the low-level dry tongues suppress the convection, rather than suppressed convection leading to drying of the lower levels of the atmosphere. The same is not true, however, for upper-tropospheric drying and moistening. Udelhofen and Hartmann (1995) used IR (11 $\mu$m) and water vapor (6.7 $\mu$m) data to study the relationship of upper-tropospheric (i.e., 550–200 mb) moistening to convective activity. They found that upper-tropospheric humidity (UTH) decreases from values of 44%–74% near the edges of upper-tropspheric clouds to 11%–15% at distances of about 500 km or more. Furthermore, they found that the ''dispersal'' of UTH from cloud edges was least for suppressed convection, and that UTH dispersal increased with increasing cloud-top height. Finally, they found that the diurnal variation of UTH lags that of upper-tropspheric cloudiness by about 8 h. Therefore, the drying of the lower and upper troposphere during the 13–16 November 1992 dry intrusion appear to be linked by convection as follows: low-level dry air suppresses convective cloud tops via enhanced stability and entrainment of dry air into convective towers, which in turn reduces the moisture source for the upper troposphere, leading to drying aloft.

The remoistening of the troposphere again is linked to convective activity. This assumption is supported by the analysis of Johnson and Lin (1997), who demonstrated that surface evaporation exceeded precipitation

[4] For days when all volumes were successfully collected, this represents 72 volumes at the analyzed 20-min resolution. Fewer than 72 volumes were analyzed on days where scheduled or unscheduled radar maintenance was performed, but these occasions were infrequent.

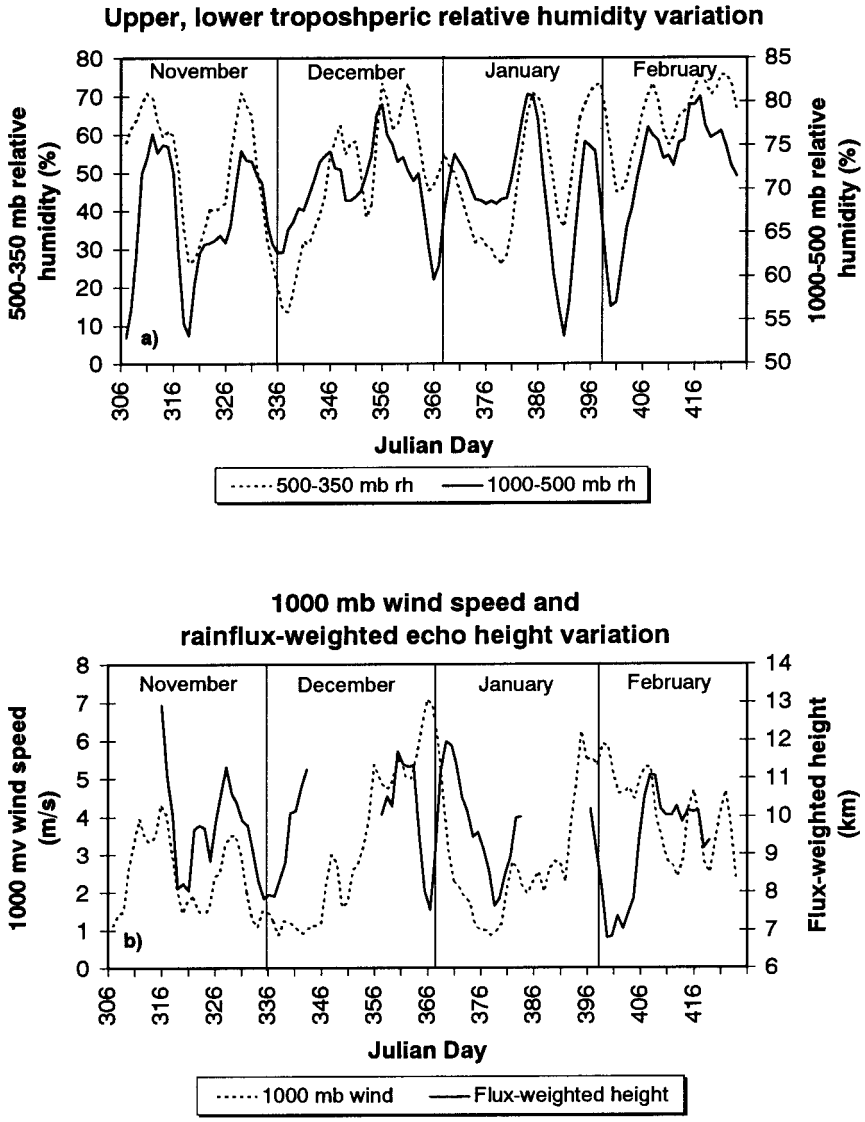


FIG. 6. Time series of (a) upper (500–350 mb) and lower (1000–500 mb) tropospheric relative humidity and (b) 1000-mb wind speed and rain flux–weighted convective grid column height during the COARE IOP. Note that the vertical axes on Fig. 6a have different values.

during this time period. Furthermore, time series of IFA-mean low-level divergence is weakly positive during this period (not shown), indicating that the remoistening was not accomplished via large-scale moisture convergence. Surface wind speeds during this period were about 2 m $s^{-1}$ and apparently provided enough moisture flux from the ocean surface to maintain convection, as evidenced by the rainfall time series shown in Part I. Moisture that is detrained from convection erodes the base of the dry layer and gradually creates a more favorable environment for subsequent deeper convection. As convection reaches higher altitudes, moistening of the upper troposphere becomes more efficient, as described in Udelhofen and Hartmann (1995). Based on the zonal wind time series cross section of Lin and Johnson (1996a), the 13–16 November 1992 dry intrusion occurred as winds associated with the early November surface westerly phase were decreasing, but before the inactive phase of the ISO was situated over the IFA. The scenario just described is quite similar to the dry intrusion of early February (Julian days 400 to about 406) described by Yoneyama and Fujitani (1995), except surface winds were stronger during this period and recovery times for tropospheric humidity are faster.

A third dry intrusion described by Numaguti et al. (1995) occurred on 25–26 November 1992 (Julian days 331–332). However, as was pointed out by Mapes and Zuidema (1996), this intrusion was sampled only by the northernmost stations composing the IFA, so its presence is not apparent in Fig. 6. Immediately following

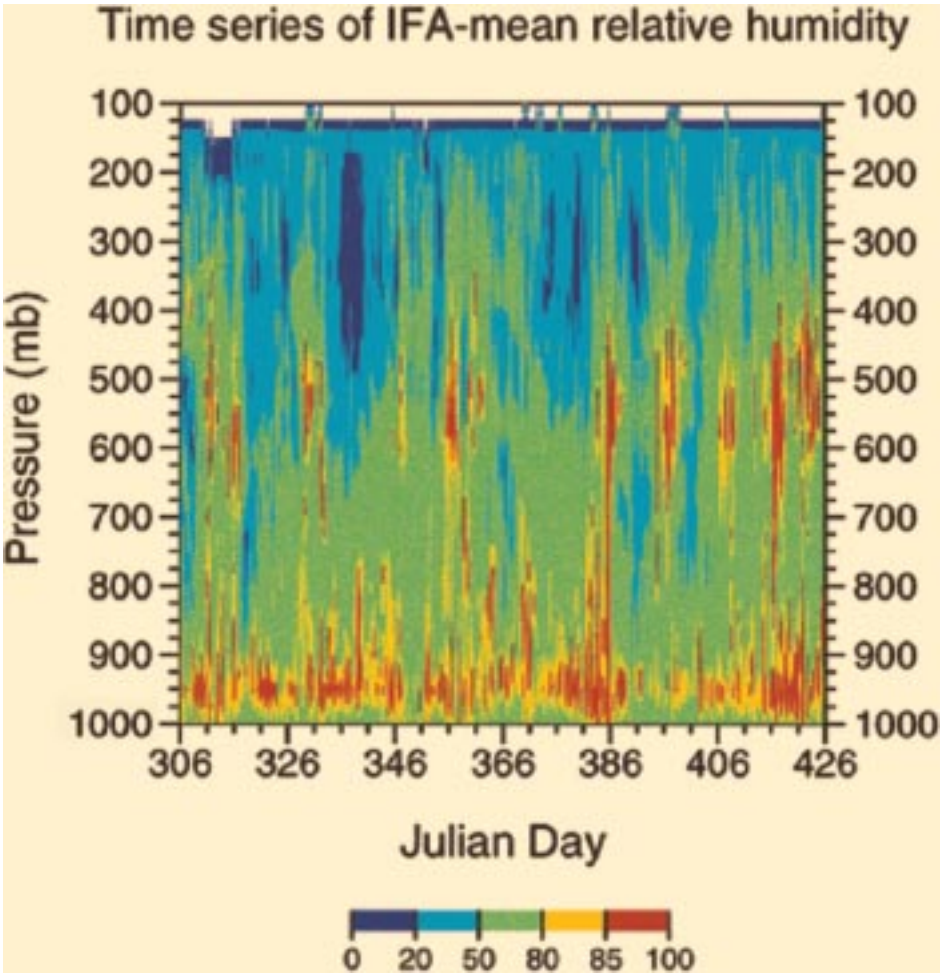


FIG. 7. Time–height cross section of tropospheric relative humidity during COARE IOP. Temporal resolution is every 6 h.

this dry intrusion, however, are decreases in upper- and lower-level relative humidities and flux-weighted cloud-top height (beginning around Julian day 336). Although the behavior of these three variables is quite similar to that discussed for the 13–16 November dry intrusion, the suppressed conditions appear to be a consequence of the inactive phase of the ISO being situated over the IFA, rather than due to suppression by a dry layer. The dramatic drying of the upper troposphere during this period is accompanied by only moderate drying of the lower troposphere (see Fig. 7). Furthermore, surface winds reach their lowest speeds observed during the entire IOP in this period (similarly low surface winds are observed in the second week of January), resulting in the lowest surface fluxes observed during the IOP (Lin and Johnson 1996b). Apparently, although surface winds are nonzero during calm surface wind conditions, owing to reduced latent heat fluxes, they were too low during the inactive phase of the Madden–Julian Oscillation (MJO) to support widespread convection.

Recovery times for both upper- and lower-relative humidity in early December is about 10 days. Flux-weighted echo top heights appear to recover somewhat faster than upper-tropospheric relative humidity, which seemingly conflicts with the conclusions of Udelhofen and Hartmann (1995) that deeper convection should moisten more efficiently than shallow convection. However, this entire 10-day period was characterized by widely spaced, isolated convective cells. Therefore, even though the convection was relatively deep, the fact that convective features were few and far between limited the rate of IFA-mean moistening in the upper troposphere. This sequence of events is consistent with the observations during the second inactive phase of the ISO that occurred in the second week of January.

The next occurrence of tropospheric drying for which convective structure data are available is the strong surface westerly period of late December–early January. The strong tropospheric shear that occurs with WWBs (50 m $s^{-1}$ over the depth of the troposphere during this period; Lin and Johnson 1996a) may suppress convective activity by inhibiting updraft strength (i.e., Weis-

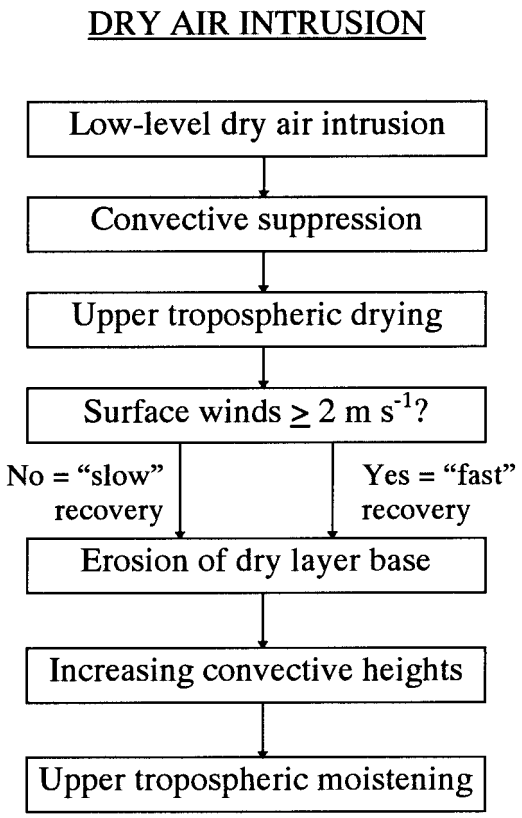


FIG. 8. Sequence of events during tropospheric drying and moistening associated with a low-level dry air intrusion.

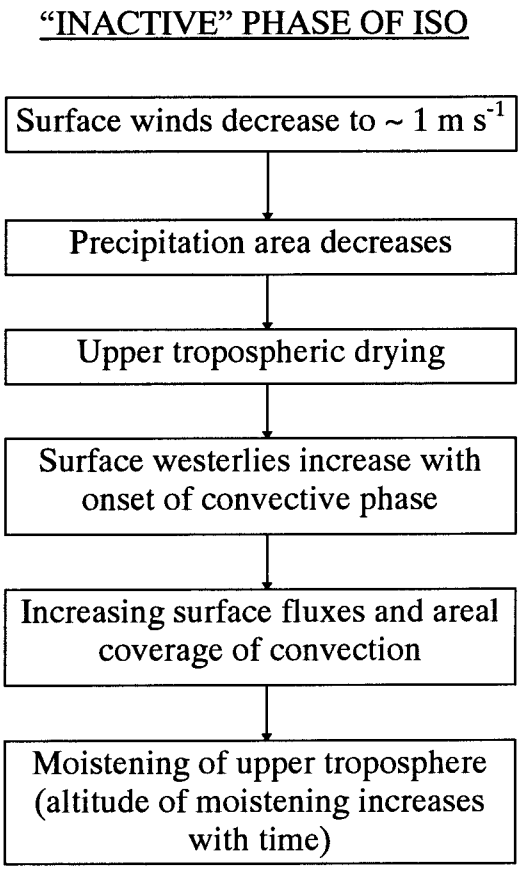


FIG. 9. As in Fig. 8 but for the ISO ''inactive'' phase.

man and Klemp 1982) and therefore its ability to organize beyond isolated convection. As with the inactive phase of the ISO, the scant and unorganized convection typical of surface westerly phases may lead to drying of the upper troposphere. However, low-level relative humidity during this period is lower than those for the inactive ISO phase ''drying'' periods (centered on Julian days 337 and 377). Sheu and Liu (1995) studied the behavior of dry intrusions during COARE using Special Sensor Microwave Imager (SSM/I) data and have attributed this low-level drying to the advection of dry subtropical air into IFA by a midlatitude cold surge, which preceded the early January surface westerly phase.

The proposed chains of events for each of the described upper-tropospheric drying mechanisms are summarized as flowcharts in Figs. 8–10. Two of the mechanisms are directly tied to the phase of the ISO, while the ''dry intrusion'' mechanism (Fig. 8) is related to higher-frequency rotational disturbances.

## 4. Convective heating profiles

The previous section discussed how convective vertical structure is modified on various spatial and temporal scales and how these modifications both impact and respond to tropospheric moisture changes. It is expected that modulations in the diabatic heating profiles accompany changes in convective vertical structure. To this end we first present a method of computing convective heating ($Q_{1c}$) profiles by combining the interpolated sounding and radar datasets, and then show how $Q_{1c}$ profiles varied from cruise to cruise. The variability of $Q_{1c}$ as a function of surface flow regime is also examined.

### *a. Computation of convective heating profiles*

Lin and Johnson (1996b) computed $Q_1$ profiles every 6 h using the interpolated sounding data. Their results provide the starting point for our diagnosis of $Q_{1c}$. The method of computation is similar to that of Yanai et al. (1973). The $Q_1$ profiles represent the combined heating from both convective and mesoscale (i.e., stratiform) precipitation. Johnson (1984) presented a method of partitioning heating profiles into convective and mesoscale components using an assumed mesoscale heating profile shape. Mathematically, $Q_1$ is the sum of the heating profiles resulting from convective, mesoscale, and radiational heating:

$$\hat{Q}_1 = f\hat{Q}_{1m} + (1 - f)\hat{Q}_{1c} + \hat{Q}_R, \qquad (2)$$

where $Q_1$ is total heating, $Q_{1c}$ is convective heating, $Q_{1m}$

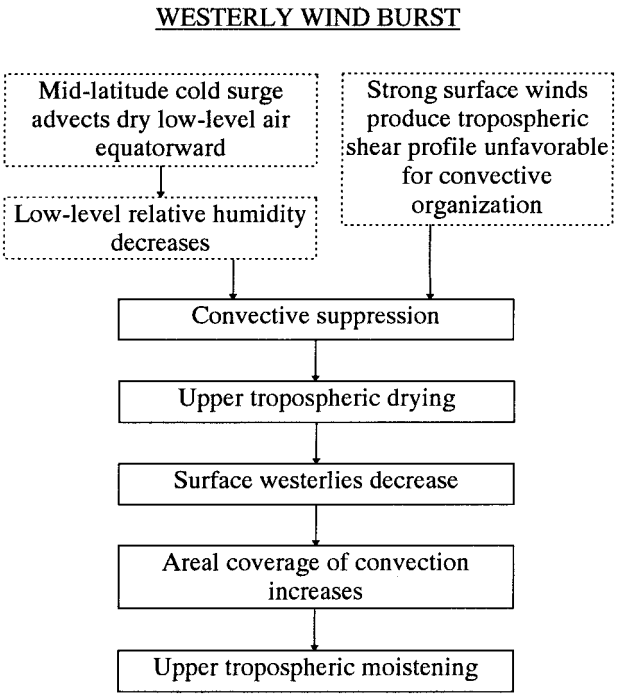


FIG. 10. As in Fig. 8 but for a surface westerly wind event. Drying associated with these events may originate with either or both of the events in the dashed-outlined boxes.

is mesoscale heating, $Q_R$ is radiational heating (longwave plus shortwave), $f$ is the fraction of total precipitation falling from mesoscale anvils (stratiform cloud), and the caret refers to normalization by rainfall rate. It should be noted that $Q_1$ and $Q_R$ are normalized by the total (convective plus stratiform) rainfall rate, $Q_{1c}$ is normalized by the convective rainfall rate, and $Q_{1m}$ is normalized by the stratiform (mesoscale) rainfall rate. Johnson (1984) computed $Q_{1c}$ profiles based on composite $Q_1$ profile presented in Yanai et al. (1973). He assumed a fixed value of $f = 0.2$ and used composite rainfall rates based on observations to normalize the heating profiles. Daily mean $Q_R$ estimates presented in Cox and Griffith (1979) were also used. Johnson's results indicate that the composite $Q_{1c}$ profile peaks at about 650 mb for $f = 0.2$, but varies between 600 and 700 mb if $f$ is allowed to vary from 0.1 to 0.3.

Equation (2) is also used to compute $Q_{1c}$ in this study, except the calculation is performed for every 6-h $Q_1$ profile from the interpolated sounding grid point closest to the R/V *Vickers* (2°S, 156°E), rather than for a time-mean composite $Q_1$ profile. An averaging time of 6 h prior to sounding launch was used to compute $f$, which represents an attempt to offset the deficiencies of the small sampling area by increasing the sampling time (and therefore the range of precipitation properties characteristic of the IFA for the sample period).

Radiative heating profile estimates were obtained from the GATE analysis of Cox and Griffith (1979) for disturbed and undisturbed conditions. The distribution of radar echo heights was used to select which profile (disturbed or undisturbed) was appropriate for each computation. Clear-sky radiative heating profiles produced by the NCAR Community Climate Model (initialized with the interpolated sounding data's temperature and moisture fields) were used when the IFA-mean brightness temperature was $\geq$275 K or when the fractional area of precipitation was $\leq$10%. Finally, the $Q_{1m}$ profile of Houze (1982) was used to complete the equation.

### b. $Q_{1c}$ profiles during COARE

Time series of daily mean $Q_{1c}$ profiles, as well as the cruise-mean average, are presented in Fig. 11. The profiles are not normalized by rainfall rate so that the variability of heating from day to day and cruise to cruise may be seen. Convective heating naturally increases during periods of heavier rainfall and tends to maximize near 750 to 500 mb. Because so many assumptions and estimates of variables go into the calculation of $Q_{1c}$, the shape of the $Q_{1c}$ profile on any given day may not be very accurate. However, many errors associated with these assumptions are probably random, so *average* profiles obtained for each cruise should be physically meaningful.

The cruise-mean $Q_{1c}$ profiles presented in Fig. 11 reveal that the vertical placement of maximum convective heating varies from cruise to cruise. The mean profiles are averages of all data points in the time series, both positive and negative. When only positive convective heating values are averaged, the magnitude of heating increases, but the overall shapes of the curves and the levels of maximum heating do not change. Similarly, eliminating Julian days 361 and 400 from the averaging results in only minor changes in the profile shapes, and has no impact on maximum heating levels. Heating (and rainfall) was greatest during cruise 2 and peaked at about 700 mb. Heating and rainfall values were lowest during cruise 1, but peak heating was shifted upward and located between 500 and 350 mb. Total heating, as well as the vertical placement of maximum convective heating for cruise 3 was in between those of cruises 1 and 2.

Because heating is related to the vertical distribution of vertical motion and to microphysical processes, it is of interest to determine how these convective heating profile shapes relate to environmental factors that may influence convective vertical motions and to the approximate microphysical structure of observed convection. Thermal buoyancy profiles (virtual temperature excess) for each cruise were computed as the difference between the virtual temperature of a parcel (with thermodynamic properties the same as the lowest 50 mb of the atmosphere) and the environment when the parcel is lifted adiabatically to its lifted condensation level, and then irreversibly lifted pseudoadiabatically to its level of neutral buoyancy (i.e., we assume all condensate falls out of the parcel as liquid water). The resultant

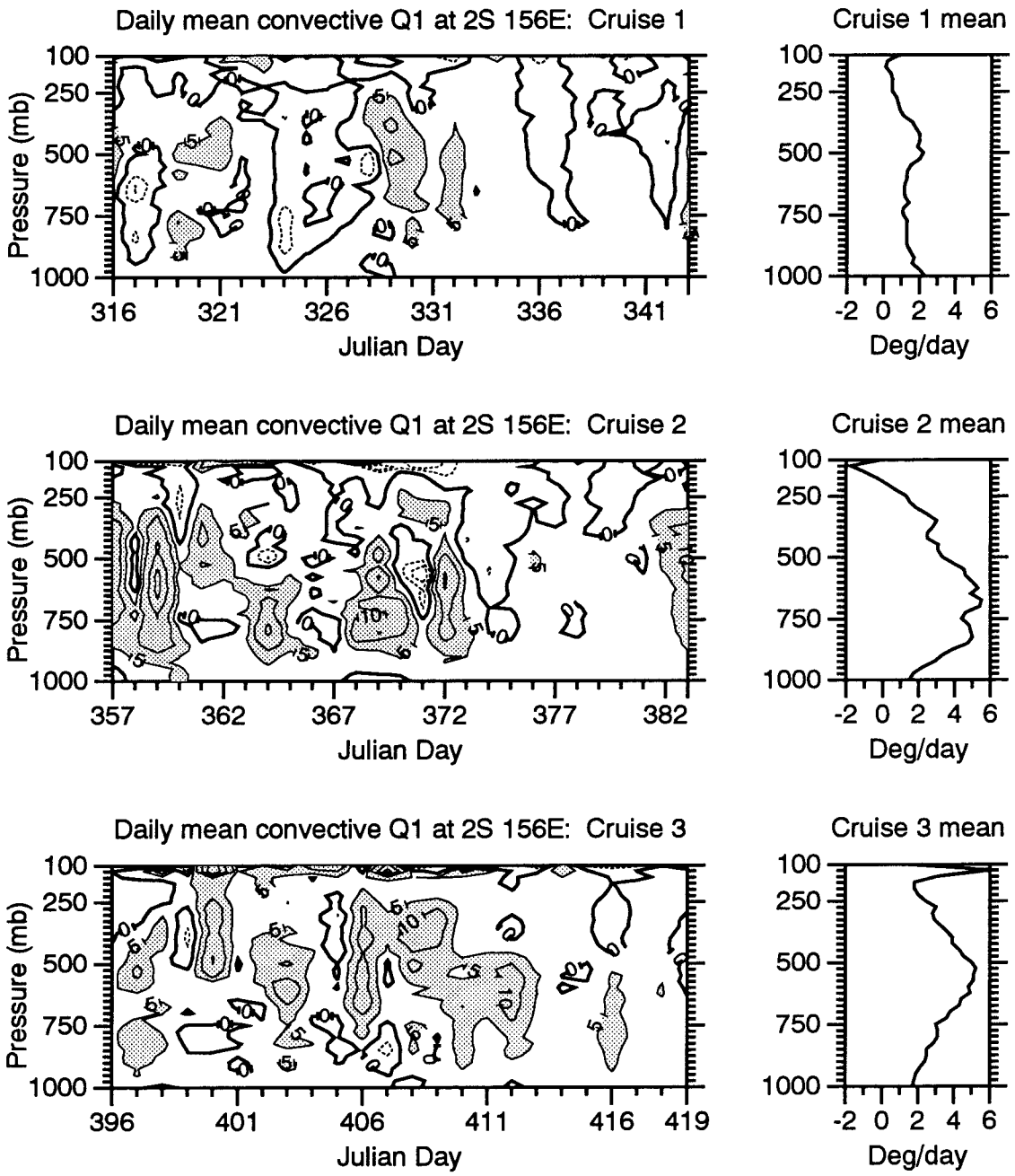


FIG. 11. Time series of convective diabatic heating ($Q_{1c}$) profiles (left panels) and mean $Q_{1c}$ profiles averaged over each cruise. Heating rates are in °C day$^{-1}$ and are contoured at −20°, −10°, −5°, 0°, 5°, 10°, 20°, and 30°C day$^{-1}$. The 0°C day$^{-1}$ contour is drawn with a heavier line and heating rates ≥5°C day$^{-1}$ are shaded.

profiles are shown in Fig. 12. Profiles for all days, as well as only those days with daily rainfall rates greater than 5 mm day$^{-1}$ were computed to aid comparisons, since both the mean convective heating profiles and mean reflectivity profiles (discussed below) are biased toward heavier rain events. For both sets of curves, buoyancy was least for cruise 2 at all levels, compared to those for cruises 1 and 3. Buoyancy profiles for cruises 1 and 3 are quite similar up to the 500-mb level, but there is slightly more buoyancy aloft during cruise 1 than during cruise 3. The fact that cruise 2 was characterized by both the lowest CAPE (the vertical integral of buoyancy) and the most convective rainfall will be discussed in the next section. For now, we wish to concentrate on differences in the shape of the buoyancy and convective heating profiles.

Vertical acceleration of an air parcel is proportional to its thermal buoyancy, or virtual temperature excess,

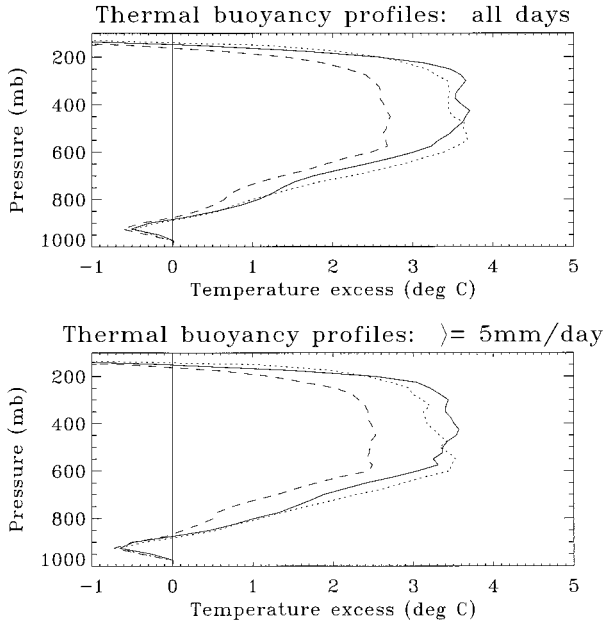


FIG. 12. Profiles of mean thermal buoyancy (defined as the difference between parcel and environmental temperatures) during COARE for (a) all days and (b) days with precipitation rates ≥5 mm day$^{-1}$: Cruise 1 (solid), Cruise 2 (dashed), and Cruise 3 (dotted).

so that a parcel that experiences a greater buoyant force will experience a larger acceleration compared to a parcel subjected to a smaller buoyancy force. Therefore, judging from the curves in Fig. 12, one would expect that on average, vertical motions during cruise 2 should be weaker than their cruise 1 and cruise 3 counterparts. Invoking the arguments of Zipser and LeMone (1980) that tropical oceanic convective updraft velocities determine convective radar reflectivity profiles, we would therefore expect convective reflectivities above the freezing level to be the lowest in cruise 2. Monthly mean convective reflectivity profiles were computed by (linearly) averaging all convective grid points at each level for each cruise. These profiles are presented in Fig. 13. It should be noted that even though cruise-to-cruise differences in mean reflectivity seldom exceed about 1.2 dB, because so many thousands of grid points go into these averages, almost any difference between the curves are statistically significant and that it is highly unlikely (probability less than 1%) that such difference arose by chance.

Differences in convective reflectivity profiles from cruise to cruise offer circumstantial evidence for the hypothesis that buoyancy, microphysical processes, reflectivity profile shape, and diabatic heating are linked. For example, cruise 2 reflectivities are uniformly weaker at all levels (except briefly near the freezing level) than those of cruise 1, and weaker than cruise 3 reflectivities below the freezing level. According to Zipser and LeMone (1980), this is physically consistent with weak convective updrafts during cruise 2 enhancing collision-coalescence processes below the freezing level and resulting in the low peak heating rates. In contrast, the greater buoyancy forces experienced at subfreezing level altitudes by rising parcels during cruises 1 and 3 would have allowed drops to grow to a larger size (resulting in the higher reflectivities) before falling as rain. Furthermore, the higher buoyancy above the freezing level in cruise 1 apparently resulted in updrafts of sufficient strength to loft supercooled liquid water above

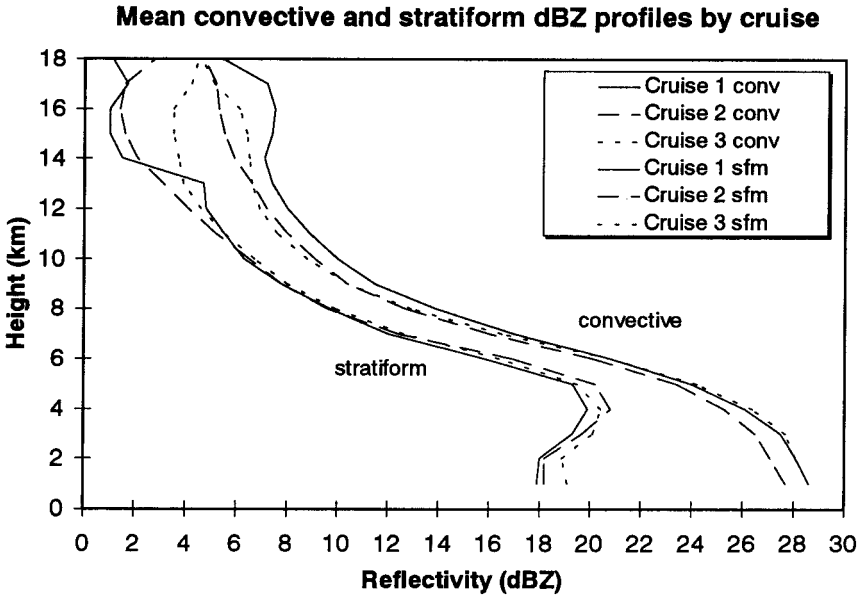


FIG. 13. Mean reflectivity profiles averaged by cruise for (a) full (unpartitioned) volumes and (b) convective and stratiform volumes.

the freezing level. Such a scenario would explain the higher reflectivity values above the freezing level for this cruise as well as the vertically higher peak heating location (as the supercooled water was converted to ice).

Given the differences in heating profile shapes and their apparent relation to the vertical distribution of buoyancy, the next logical question to ask is what controls the buoyancy distribution in easterly and westerly surface flow regimes. As Lin and Johnson (1996a) have demonstrated, sea surface temperatures during the inactive (usually easterly surface flow) phase of the ISO are 1°–1.5°C higher than during westerly surface flow associated with the convectively active and surface westerly phases of the ISO. The warmer ocean temperatures translate to a warmer boundary layer, thus increasing the potential buoyancy of near-surface parcels. The presence of stable layers in the TOGA COARE region (Johnson et al. 1996) can also affect buoyancy profiles, although there is insufficient evidence in the literature to determine the relative importance of the type of stable layer present versus surface moisture conditions.

## 5. Summary

Variations of convective activity, as indicated by time series of rainfall and convective echo distributions, were examined with respect to their response to, and impact on, environmental variables. Daily mean distributions of convective heights and 30-dB*Z* heights reveal that at least some deep convection was always present, even during periods when overall convective activity was quite low. Modal convective heights varied from less than 5 km to 13 km over the course of just one day. Variability of 30-dB*Z* contour height distributions were not as dramatic, but varied in a manner temporally similar to those of echo top heights. Convective rainfall was often produced by two different populations of convective cloud, one deep and vertically intense, and another that was shallow and less vertically intense, although it appears that these two populations did not exist simultaneously. Convective heights and 30-dB*Z* contour heights were substantially suppressed during surface westerly phases and, at least in the two convective-surface westerly cycles sampled, reached their maximum vertical development as surface winds associated with the WWB decreased and not during the passage of the main convective phase of the ISO.

Suppression of convective heights was associated with three distinct phenomena: low-level intrusions of subtropical dry air into the IFA, low surface wind speeds characteristic of the inactive phase of the ISO, and strong surface westerlies. In each case, suppression of convective vertical development led to upper-tropospheric drying. Convective heights increased and upper-tropospheric moistening resumed as the ''suppressing'' condition weakened (i.e., as the low-level dry tongue was eroded by detraining water vapor from its base upward, or as surface winds increased or decreased for inactive and surface westerly phases of the ISO, respectively).

Profiles of convective diabatic heating were computed using a combination of sounding-derived total diabatic heating, radar-derived rainfall amounts, and idealized and calculated radiative heating profiles. Instantaneous convective heating estimates are subject to potentially large, but probably random errors, so the results are physically meaningful when averaged over many days. Cruise-mean convective heating profiles reveal variations in the placement of maximum heating for each cruise, which are qualitatively consistent with the cruise-mean buoyancy profiles and likely microphysical processes based on mean reflectivity profile shape. The data analyzed in this study suggest that the ''internal'' structure of convection may be a better indicator of diabatic heating profile shape than cloud-top height. Factors that may control the vertical distribution of buoyancy (and apparently heating profiles, too) are warmer sea surface temperatures characteristic of the inactive phase of the ISO, sampled during cruise 1, and possibly stronger midlevel stable layers during the active ISO phase, sampled during cruise 2.

*Acknowledgments.* Support for this work was provided by NASA Graduate Fellowship on Global Change NGT-30099 SUPP 3 and by NASA TRMM Grant NAG-5-2692. We extend special thanks to Dr. Richard Johnson, Mr. Paul Ciesielski, and Dr. Xin Lin of Colorado State University for providing analysis products based on the interpolated sounding dataset, as well as their many helpful discussions and suggestions during the course of this work. We gratefully acknowledge all of those who worked so hard before, during, and after COARE to make the shipboard radar program a success.

## REFERENCES

Black, R. A., 1990: Radar reflectivity-ice water content relationships for use above the melting level in hurricanes. *J. Appl. Meteor.*, **29,** 955–961.

Byers, H. R., and R. R. Braham, 1949: The thunderstorm project. U.S. Weather Bureau, U.S. Dept. of Commerce, Washington, DC, 287 pp. [NTIS PB234515.]

Carey, L. D., and S. A. Rutledge, 1996: A multiparameter radar case study of the microphysical and kinematic evolution of a lightning producing storm. *Meteor. Atmos. Phys.*, **59,** 33–64.

Chen, S. S., R. A. Houze Jr., and B. E. Mapes, 1996: Multiscale variability of deep convection in relation to large-scale circulation in TOGA COARE. *J. Atmos. Sci.*, **53,** 1934–1945.

Cox, S. K., and K. T. Griffith, 1979: Estimate of radiative divergence during Phase III of the GARP Atlantic Tropical Experiment: Part II. Analysis of the Phase III results. *J. Atmos. Sci.*, **36,** 586–601.

French, J. R., J. H. Helsdon, A. G. Detwiler, and P. L. Smith, 1996: Microphysical and electrical evolution of a Florida thunderstorm. Part I: Observations. *J. Geophys. Res.*, **101,** 18 961–18 977.

Haertel, P. T., and R. H. Johnson, 1998: Two-day disturbances in the equatorial western Pacific. *Quart. J. Roy. Meteor. Soc.*, in press.

Houze, R. A., Jr., 1982: Cloud clusters and large-scale vertical motions in the Tropics. *J. Meteor. Soc. Japan,* **60,** 396–410.

——, 1989: Observed structure of mesoscale convective systems and

implications for large-scale heating. *Quart. J. Roy. Meteor. Soc.*, **115,** 425–461.

Jameson, A. R., M. J. Murphy, and E. P. Kriden, 1996: Multiple-parameter radar observations of isolated Florida thunderstorms during the onset of electrification. *J. Appl. Meteor.*, **35,** 343–354.

Johnson, R. H., 1984: Partitioning tropical heat and moisture budgets into cumulus and mesoscale components: Implications for cumulus parameterization. *Mon. Wea. Rev.*, **112,** 1590–1601.

——, and G. S. Young, 1983: Heat and moisture budgets of tropical mesoscale clouds. *J. Atmos. Sci.*, **40,** 2138–2147.

——, and X. Lin, 1997: Episodic trade wind regimes over the western Pacific warm pool. *J. Atmos. Sci.*, **54,** 2020–2034.

——, P. E. Ciesielski, and K. A. Hart, 1996: Tropical inversions near the 0°C level. *J. Atmos. Sci.*, **53,** 1838–1855.

Jorgensen, D. P., and M. A. LeMone, 1989: Vertical velocity characteristics of oceanic convection. *J. Atmos. Sci.*, **46,** 621–640.

Lau, K.-M., L. Peng, C. H. Sui, and T. Nagazawa, 1989: Dynamics of super cloud clusters, westerly wind bursts, 30–60 day oscillations and ENSO: A unified view. *J. Meteor. Soc. Japan,* **67,** 205–219.

Lhermitte, R., and E. Williams, 1985: Thunderstorm electrification: A case study. *J. Geophys. Res.*, **90,** 6071–6078.

Lin, X., and R. H. Johnson, 1996a: Kinematic and thermodynamic characteristics of the flow over the western Pacific warm pool during TOGA COARE. *J. Atmos. Sci.*, **53,** 695–715.

——, and ——, 1996b: Heating, moistening, and rainfall over the western Pacific warm pool during TOGA COARE. *J. Atmos. Sci.*, **53,** 3367–3383.

Lucas, C., E. J. Zipser, and M. A. LeMone, 1994: Vertical velocity in oceanic convection off tropical Australia. *J. Atmos. Sci.*, **51,** 3183–3193.

Mapes, B. E., and P. Zuidema, 1996: Radiative-dynamical consequences of dry tongues in the tropical troposphere. *J. Atmos. Sci.*, **53,** 620–638.

Numaguti, A., R. Oki, K. Nakamura, K. Tsuboki, N. Misawa, T. Asai, and Y.-M. Kodama, 1995: 4–5-day-period variation on low-level dry air observed in the equatorial western Pacific during the TOGA COARE IOP. *J. Meteor. Soc. Japan,* **73,** 267–290.

Petersen, W. A., S. A. Rutledge, and R. E. Orville, 1996: Cloud-to-ground lightning observations from TOGA COARE: Selected results and lightning location algorithms. *Mon. Wea. Rev.*, **124,** 602–620.

Ramachandran, R., A. Detwiler, J. Helsdon, P. L. Smith, and V. N. Bringi, 1996: Precipitation development and electrification of Florida thunderstorm cells during Convection and Precipitation/Electrification Project. *J. Geophys. Res.*, **101,** 1599–1619.

Reed, R. J., and E. E. Recker, 1971: Structure and properties of synoptic-scale wave disturbances in the equatorial western Pacific. *J. Atmos. Sci.*, **28,** 1117–1133.

Rutledge, S. A., E. R. Williams, and T. D. Keenan, 1992: The Down Under Doppler and Electricity Experiment (DUNDEE): Overview and preliminary results. *Bull. Amer. Meteor. Soc.*, **73,** 3–16.

Sheu, R.-S., and G. Liu, 1995: Atmospheric humidity variations associated with westerly wind bursts during Tropical Ocean Global Atmosphere (TOGA) Couple Ocean Atmosphere Response Experiment (COARE). *J. Geophys. Res.*, **100,** 25 759–25 768.

Szoke, E. J., E. J. Zipser, and D. P. Jorgensen, 1986: A radar study of convective cells in mesoscale systems in GATE. Part I: Vertical profile statistics and comparison with hurricanes. *J. Atmos. Sci.*, **43,** 181–197.

Takahashi, T., 1978: Electrical properties of oceanic tropical clouds at Ponape, Micronesia. *Mon. Wea. Rev.*, **106,** 1598–1612.

Takayabu, Y. N., K.-M. Lau, and C.-H. Sui, 1996: Observation of a quasi two-day wave during TOGA COARE. *Mon. Wea. Rev.*, **124,** 1892–1913.

Udelhofen, P. M., and D. L. Hartmann, 1995: Influence of tropical cloud systems on the relative humidity in the upper troposphere. *J. Geophys. Res.*, **100,** 7423–7440.

Ushiyama, T., S. Sath, and K. Takeuchi, 1995: Time and spatial variations of mesoscale rainfalls and their relation to the large-scale field in the western tropical Pacific. *J. Meteor. Soc. Japan,* **73,** 379–391.

Weisman, M. L., and J. B. Klemp, 1982: The dependence of numerically simulated convective storms in vertical wind shear and buoyancy. *Mon. Wea. Rev.*, **110,** 504–520.

Wong, T., G. L. Stephens, and P. W. Stackhouse Jr., 1993: The radiative budgets of a tropical mesoscale convective system during the EMEX-STEP-AMEX Experiment. Part II: Model results. *J. Geophys. Res.*, **98,** 8695–8711.

Yanai, M., S. Esbensen, and J. H. Chu, 1973: Determination of bulk properties of tropical cloud clusters from large-scale heat and moisture budgets. *J. Atmos. Sci.*, **30,** 611–627.

Yoneyama, K., and T. Fujitani, 1995: The behavior of dry westerly air associated with convection observed during the TOGA-COARE R/V *Natsushima* cruise. *J. Meteor. Soc. Japan,* **73,** 291–304.

Zipser, E. J., and M. A. LeMone, 1980: Cumulonimbus vertical velocity events in GATE. Part II: Synthesis and model core structure. *J. Atmos. Sci.*, **37,** 2458–2469.

——, and K. R. Lutz, 1994: The vertical profile of radar reflectivity of convective cells: A strong indicator of storm intensity and lightning probability? *Mon. Wea. Rev.*, **122,** 1751–1759.